LASER & PHOTONICS REVIEWS
www.lpr-journal.org

Multiple High-*Q* Optical Modes in a Polymer-Lithium Niobate Integrated Metasurface

Cizhe Fang, Ruoying Kanyang, Yingke Ji, Yong Zhang, Jiayong Yang, Di Wang, Yan Liu, Xuetao Gan,* Genquan Han, and Yue Hao*

With the development of miniaturization and integration, multifunctional optical devices are necessary. However, its practical realization is a critical challenge due to the lack of simple structures with multiple functionalities. Here, a multimode metasurface is proposed by simply placing polymer nanocubes on the lithium niobate (LN) thin film. The intriguing properties of the integrated structure include high-quality (*Q*) factors and different spectral characteristics, associated with quasi-guide modes (GM) and Mie modes, respectively. The experiment demonstration reveals that *Q* factors of four modes are larger than 1000 and a second harmonic generation (SHG) enhancement factor of 25.4 is obtained, featuring strong light-matter interaction. Importantly, the abundant spectral characteristics greatly boost three degrees of freedom, i.e., polarization, incident angle, and slot, to realize multifunctional designs. The results provide a sophisticated platform for developing high-performance LN metasurfaces with the advantages of simplified fabrication processes and multifunctionality. The strategy can also be extended to other material systems, enabling the flexibility of metasurface-inspired subwavelength engineering.

1. Introduction

Modern optics aims to integrate diverse functionalities into a single device, enabling compact integration and miniaturization in photonics.[1,2] The concept of metasurfaces facilitates achieving this goal for its small footprint and ease of integration.[3–5] Metasurfaces, ultrathin planar arrays of artificial subwavelength elements, have been rapidly developed for their powerful capability to manipulate light.[6–10] However, the metasurface proposed so far only achieves one specific function due to the determination of their geometric structure and material selection. The concept of active metasurfaces is driven by the idea of integrating passive metasurfaces with various active components (e.g., transistors, varactors, etc.).[11–14] Though active metasurfaces realize tunable or switchable functionalities, their multifunctionality is still limited by the initial spectral characteristics, accompanied by higher system complexity. A simple structure is highly desired for achieving multifunctional metasurfaces.

Recently, many efforts have been devoted to optical multiplexing to achieve the multifunctional metasurface.[2,15] Polarization, wavelength, and incident angle, input parameters of a given light source, are taken as multiplexing channels. In this sense, a multimode metasurface is of fundamental importance for the realization of the multifunction design. Mie modes are been mostly concerned because they support multipole resonances,[11,16,17] which can avoid functional crosstalk in interleaved configurations.[2,15] However, the strength of higher-order multipoles is generally weak, thus complex designs are adopted.[18–21] It may be challenging to implement for practical applications. An alternative solution is to introduce other types of modes, such as guide mode,[22,23] Fabry-Perot modes,[24] and surface lattice resonances.[25,26] In these scenarios, the focus is mainly put on the interaction between different modes like coupling[23,25–27] or suppressing,[28] thus performing a monofunctionality or similar functionalities.[29] It is rarely reported that different types of modes coexist in a simple structure,[30] as well as the relationship between the degrees of freedom and functionality.

In this paper, we propose a multimode metasurface consisting of polymer nanocubes and the LN thin film. LN is an ideal platform for light-matter interactions for its wide transmission window.[31] An important approach of our study is the introduction of polymer nanocubes. It not only couples the guide mode to the far field but also enhances Mie modes. Assisted by the anisotropy of the LN, the proposed structure can support four different optical modes. The optical characteristics of these modes are thoroughly studied by theoretical analysis and

C. Fang, R. Kanyang, Y. Zhang, J. Yang, D. Wang, Y. Liu, G. Han, Y. Hao
Hangzhou Institute of Technology
Xidian University
Hangzhou 311200, China
E-mail: xdliuyan@xidian.edu.cn

C. Fang, R. Kanyang, Y. Zhang, J. Yang, D. Wang, Y. Liu, G. Han, Y. Hao
School of Microelectronics
Xidian University
Xi'an 710071, China

Y. Ji, X. Gan
Key Laboratory of Light Field Manipulation and Information Acquisition
Ministry of Industry and Information Technology, and Shaanxi Key Laboratory of Optical Information Technology
School of Physical Science and Technology
Northwestern Polytechnical University
Xi'an 710129, China
E-mail: xuetaogan@nwpu.edu.cn

The ORCID identification number(s) for the author(s) of this article can be found under https://doi.org/10.1002/lpor.202300900

DOI: 10.1002/lpor.202300900

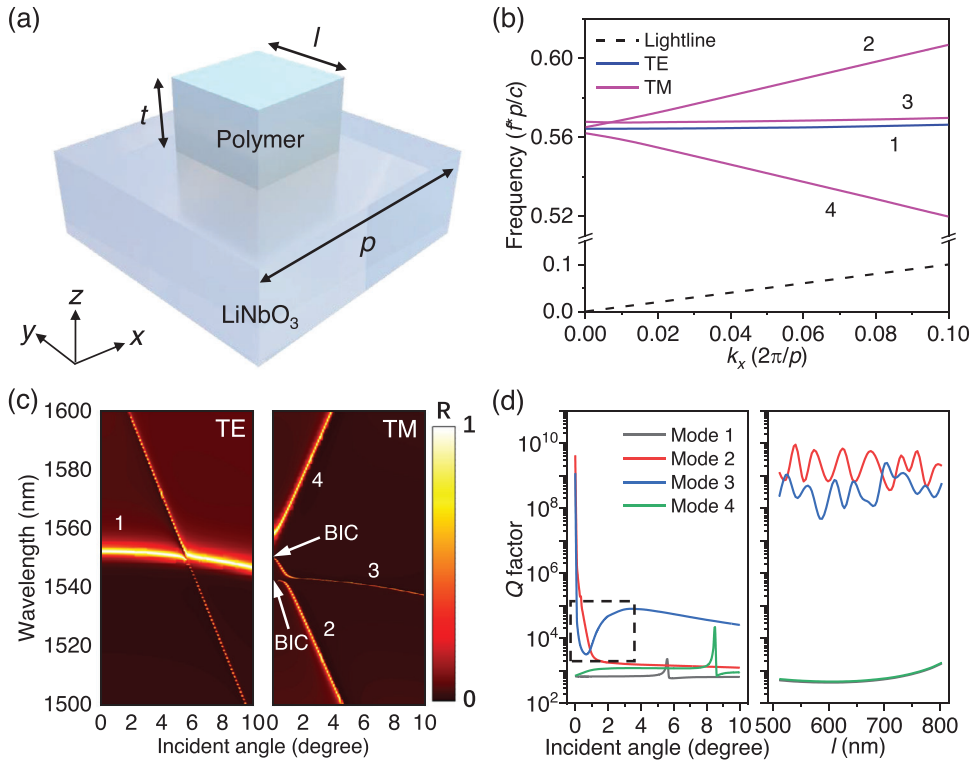

Figure 1. a) 3D Schematic of the polymer-LN composite unit cell. b) Dispersion curves for the polymer nanocube in square lattice placed on LN thin film. TE and TM modes are marked by blue and pink solid lines, respectively. The light line is labeled as the black dashed line. c) Angle-resolved reflection spectra for the TE/TM-polarized incidence. d) Calculated *Q* factor as a function of the incident angle (left panel) and length *l* (right panel) for Mode 1–4. The incident angle corresponds to the Γ-*X* direction.

experiment measurements, as well as the nonlinear effect. Moreover, the mode selection in the integrated metasurface is discussed to achieve multifunctionality. The proposed strategy provides a simple approach for practical devices with multifunctionalities based on LN.

2. Structure Design and Theoretical Analysis

Figure 1a schematically illustrates a polymer nanocube located on the LN thin film. It has a thickness of t and a length of l. A clever arrangement should be taken to excite/enhance more resonance modes. For in-plane lattice propagation, the propagation constant β must satisfy the following relationship:

$$k_0 n_{\text{sub}} \leq \left| Re\{\beta\} \right| < k_0 n_{\text{eff}}. \quad (1)$$

Here k_0 is the incident wavevector, and n_{sub} and n_{eff} are the effective refractive index of the substrate and the unit cell, respectively. For normal incidence, Equation 1 is simplified to

$$n_{\text{sub}} \leq \frac{\lambda}{p}\sqrt{m^2 + n^2} < n_{\text{eff}} \quad (2)$$

where m and n are diffracting orders in the x- and y- directions, respectively. To obtain the resonance modes in the telecom C-band, the square lattice p is set as 876 nm.

With the eigenmode analysis based on the finite element method (see Experimental Section for details), the dispersion curve is calculated after an elaborate geometric design (l = 730 nm, p = 876 nm, t = 400 nm). As shown in Figure 1b, four modes appear above the lightline. For clarity, these modes are marked as Mode 1–4. The angle-resolved reflection spectra excited by transverse electric (TE) and transverse magnetic (TM) polarized wave are shown in Figure 1c. Each mode has a different spectral response to the incident angle. For Mode 1, the resonance is relatively stable, whose spectral linewidth remains unchanged as the incident angle increases. Mode 4 behaves similarly, though its spectral linewidth is slightly narrower. Unlike Mode 1, the resonance wavelength of Mode 4 redshifts more than 40 nm with the incident angle varying from 0° to 4°. Mode 2 and 3 are sensitive to the incident angle at a tiny window in the vicinity of the normal incidence. Their reflection spectra exhibit narrow peaks that vanish when the incident angle is 0°. Notably, the resonance of Mode 3 sustains a small linewidth even at large incident angles.

For better understanding, we calculate the *Q* factors and model them as a function of the incident angle and length *l*, respectively. In Figure 1d, two important features are identified: 1) For Mode 1 and Mode 4, the *Q* factors have a weak dependence on both the incident angle and *l*, which remain ≈10^3; 2) Mode 2 and Mode 3 are extremely sensitive to the incident angle. As the incident angle increases from 0° to 0.1°, the *Q* factor drops from ≈10^9 to ≈10^6 (Mode 2) and ≈10^4 (Mode 3). The anomalous region of the blue

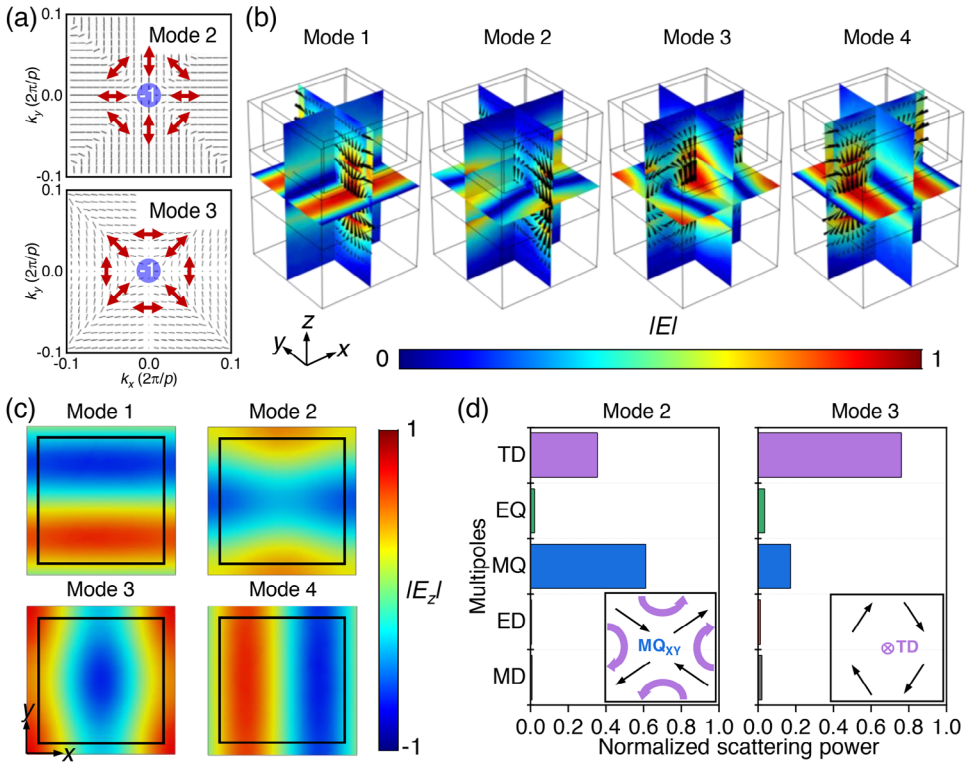

Figure 2. a) The polarization vector field and its corresponding topological charge at the Γ point for Mode 2 and Mode 3. b) Numerically calculated electric cross sections under the normal incidence of the corresponding polarized wave for Mode 1–4. The electric field vectors are denoted by black cones. The layers are polymer, LN, and SiO_2 from top to bottom. c) E_z distribution in the *x*-*y* plane for Mode 1–4. d) The multipole decomposition of the composite unit cell for Mode 2 (left) and Mode 3 (right). The scattering power includes the magnetic dipole (MD), electric dipole (ED), magnetic quadrupole (MQ), electric quadrupole (EQ), and toroidal dipole (TD) moments. The inset shows the representation of the MQ and TD in terms of the MDs within the *x*-*y* plane.

curve (indicated by the black dashed box) results from the interference between Mode 2 and Mode 3. Despite the drastic change, the *Q* factors of Mode 2 and Mode 3 maintain ultrahigh values (≈10^9), generally regarded as an infinite value owing to computational constraints. Mode 2 and Mode 3 are sensitive to the symmetry perturbation (i.e., the incident angle) while independent of the geometrical perturbation *l*, a typical characteristic of the symmetry-protected bound state in the continuum (BIC).[32–34]

To verify the above-mentioned speculation, the far-field polarization plots are calculated and shown in **Figure 2**a (see Section I in Supporting Information). For both modes, there exist vortices around the Γ points and the polarization directions are ill-defined at the Γ points, corresponding to the nature of singularities in momentum space.[33,35–37] The topological charge *q* carried by the resonance mode is evaluated by[36]

$$q = \frac{1}{2\pi} \oint_C dk \cdot \nabla_k \phi(k) \tag{3}$$

Here $\boldsymbol{k}$ is the wave vector and (k) is the angle of the polarization vector. *C* is a closed counterclockwise loop around the Γ point in $\boldsymbol{k}$ space. Both Mode 2 and Mode 3 are BIC since they appear as topological vortexes with an integer topological charge of −1.

To further interpret the underlying mechanism, four modes are analyzed with the electric field profile. According to Figure 2b, Mode 1 originates from the GM. The conventional GM is completely confined in a slab and thus inaccessible from the far field.[38,39] Here, polymer nanocubes act as a periodic grating. With periodic corrugation, the dispersion curves are folded into the first Brillouin zone. As shown in Figure 2c, the E_z field distribution is odd under C_2^z rotations, signifying that the GM can couple to the far field. That is, the GM scatters out via polymer nanocubes and transforms into a leaky mode, noted as quasi-GM. Mode 4 has a similar electric field distribution, also identified as quasi-GM. The only difference is the polarization configuration. For TE incidence, the transverse electric component always remains the same (i.e., along the *y*-axis); while for TM incidence, it continuously varies with the incident angle. Therefore, Mode 4 is found to exhibit an extraordinary spectral sensitivity to small changes in the incident angle (see Figure 1c). Indeed, the *Q* factors of Mode 1 and Mode 4 can be modulated by adjusting the materials and dimensions of nanocubes.[40,41]

The field distributions of Mode 2 and Mode 3 indicate a clear combination of Mie mode and lattice effect (for details, see Supporting Information). The electric field vectors induce four MDs within the *x*-*y* plane for both Mode 2 and Mode 3. For Mode 2, these MDs can be equivalent to two pairs of MQs, i.e., antiphase MDs,[42–44] inside the unit cell. Simultaneously, the MDs are also circulating between neighboring unit cells, forming TDs along the *z*-axis.[45–47] To assess the weights of the multipolar composition, the multipole expansion is calculated (see Section II in Supporting Information). Figure 2d shows that Mode 2 mainly

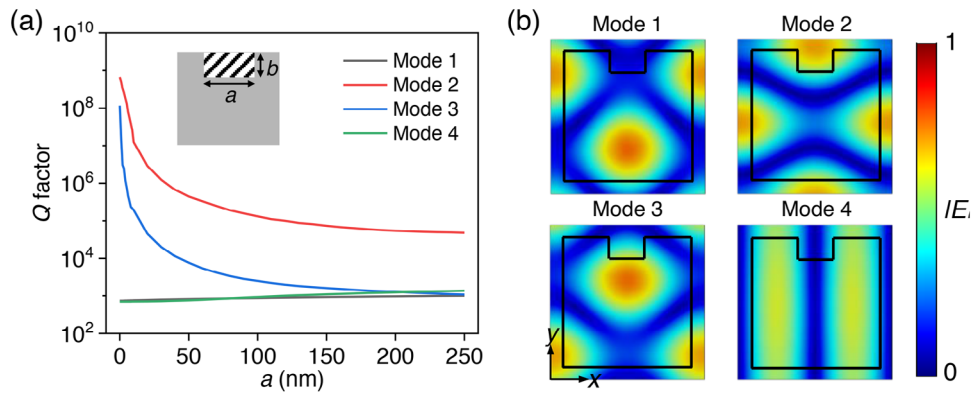

Figure 3. a) Calculated Q factor as a function of the slot width a for Mode 1–4. Inset: the diagrammatic sketch of the slot. b) Electric field distribution in the x-y plane for Mode 1–4 after introducing the slot. The width and depth of the slot are 150 and 120 nm, respectively. The boundary of the nanocube is denoted by the black line.

originates from the MQ moment (62%), indicative of MQ-BIC. MDs form a head-to-tail close loop within the unit cell for Mode 3, generating the TD along the z-axis. A coupling between neighboring unit cells produces the MQ in the x-y plane. The contribution of the TD moment reaches 77%, namely TD-BIC. The field distributions of both modes are even under C^2_z rotations in Figure 2c, so the TD moment does not radiate along the z-axis.[47,48] The radiation of the MQ in the transverse plane can also be negligible due to the compensation effect of the periodic array.[49] Given contributions of the ED, MD, and EQ moments are nearly zero, Mode 2 and Mode 3 have zero radiation loss. Note that, they exhibit different mode distributions, which affects their spectral responses to the incident angle. Further discussion is presented in Supporting Information Section IV.

Compared with the incident angle, the structural defect can be a more effective approach to tuning spectral responses. A slot with a width of a and a depth of b is introduced in the composite unit cell. **Figure 3**a compares the Q factor dependence on the slot size. Due to the existence of the radiative channel, Mode 1 and Mode 4 hold relatively small Q factors. As the quasi-guided mode, Mode 1 and Mode 4 are insensitive to the perturbation. Both Q factors and mode distributions are varied lightly. Despite owning infinite Q factors at $a = 0$ nm, Mode 2 and Mode 3 behave differently as a increases. The electric field is confined in the inner unit cell for Mode 3 while located at the boundary of the unit cell for Mode 2. As the slot is introduced, the mode leakage is more serious for Mode 3, as shown in Figure 3b. Consequently, the Q factor of Mode 3 has an obvious variation with the change in a. The effective perturbation volume plays the dominant role in governing the Q factors.

3. Experimental Results and Discussions

On the basis of the above analysis, polymer nanocubes are fabricated on the lithium-niobate-on-insulator (LNOI) substrate using only one step of electron-beam lithography. Analysis of the scanning electron microscopy (SEM) confirms that the morphology of nanocubes is well-defined and the distribution of nanocube size has good uniformity (see Figure S3 in Supporting Information). The fabricated samples are measured in a home-built setup with a reflection configuration. Microscope objectives with different numerical apertures (NA) are utilized to characterize the linear and nonlinear optical characterizations. Detailed information on sample fabrication and characterization is presented in the Experimental Section.

For better characterizing BIC modes, a 2×/0.055 NA microscope objective is utilized so that the laser beam is focused on the sample with a small k_x (nearly zero). The interferences from other wavevectors are reduced to minimum. The measured result agrees excellently with the predictions from our simulations. As shown in **Figure 4**a, four resonances are observed, corresponding to Mode 1–4. A slot is introduced as the symmetry perturbation. We measure the reflection spectra of the samples with different slot widths (see Figure S4 in Supporting Information). The Q factors are extracted and shown in Figure 4b. For Mode 1, the Q factor is relatively small and increases slightly (from ≈700 to ≈1000) along with the slot width a. A similar transition occurs for Mode 4, whose Q factor is nearly the same as that of Mode 1. Contrastingly, it shows an obvious degeneration in Q factors with increasing a for both Mode 2 and Mode 3. The Q factor of Mode 2(3) drops from 3425(2565) to 920(940) as a varies from 0 to 252 nm. The above results are consistent with the simulation results, confirming that the slot can be a degree of freedom to adjust to manipulate spectral characteristics.

Note that measured Q values exhibit both radiative (Q_r) and non-radiative (Q_{nr}) contributions (e.g., lateral leakage and fabrication imperfections), i.e., $Q^{-1} = Q_r{}^{-1} + Q_{nr}{}^{-1}$. .[34,50,51] As for Mode 1 and Mode 4, despite the device fabrication induces the Q_{nr} contribution, the initial radiative channel (i.e., polymer nanocubes) still dominates the leakage loss. Therefore, the measured Q factors differ little from the theoretical ones. In contrast, the radiative loss Q_r is small for Mode 2 and Mode 3. The experimental Q factors are dominated by Q_{nr}. Since the lateral leakage and fabrication imperfections are inevitable, the Q factors are not infinite even in the samples without slot (i.e., $a = 0$ nm). Given the BIC mode is sensitive to the perturbation, the experimental Q factors differ from the theoretical results. The process variations aggravate this deviation, especially at small values of a. The theoretically predicted Q factors can be used to evaluate the availability of the structure design. To improve the Q factor, the process should be further optimized to scale down the slot and reduce fabrication imperfections. Considering slot stability, slot width a is designed

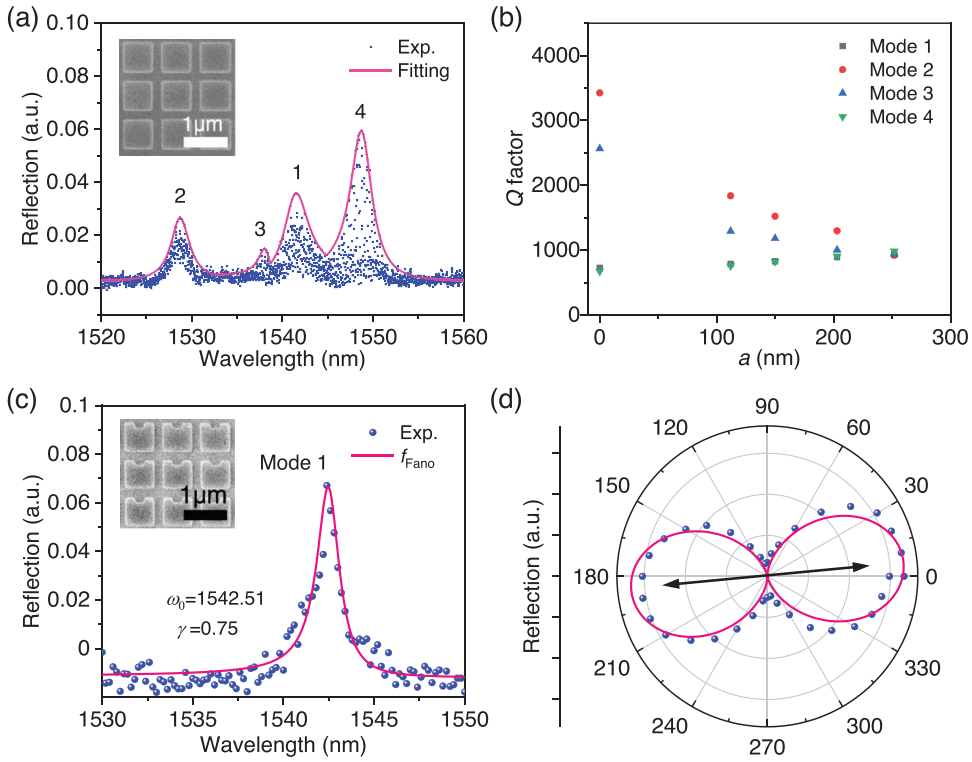

Figure 4. a) Measured reflection spectrum for the fabricated sample. The geometrical parameters are lattice constant $p = 876$ nm, length $l = 660$ nm, and thickness $t = 400$ nm. Inset: SEM image of nanocubes without slot. b) Q factor characterization of the samples with different slot widths (slot depth $b = 120$ nm). c) The reflection spectrum with the highest Q factor for Mode 1 (150 × 150). Inset: SEM image of nanocubes with slot. The geometrical parameters of the slot are $a = 200$ nm and $b = 120$ nm. d) Normalized polarization-dependent reflected intensities with the excitation of an on-resonance laser. The black arrow indicates the y-direction.

larger than 100 nm, which has room to scale down. In addition, more strategies can be adopted, like a zigzag array, to avoid the geometrical defect.[33]

As a material possessing excellent second-order nonlinear susceptibility, we now investigate the SHG in this LN-based integrated structure.[52,53] Considering that the harmonic signal is weak and a small NA microscope objective has poor collection capability, a large NA (20×/0.4) microscope objective is utilized. Accordingly, BIC modes (i.e., Mode 2 and Mode 3) are not suitable for SHG characterization despite they may achieve larger SHG enhancement owing to their large Q factors. The second-order nonlinear polarization is written as $P^{(2)}{}_{SHG} = X^{(2)} E^2$, where $X^{(2)}$ is second-order nonlinear susceptibility. The intensity of the electric field plays an important role in boosting SHG. To take advantage of the largest nonlinear coefficient, an incident beam should polarize along the optical axis (i.e., y-direction in this work) of LN. Therefore, Mode 1 is chosen for SHG emission since its resonant field concentration occurs in the direction parallel to the optical axis. After optimizing the structural parameters, the sample with an array size of 150 × 150 is fabricated. The influence of the array size on the Q factor is discussed in Supporting Information Section VII. Figure 4c shows the measured reflection spectrum of Mode 1. A high Q factor of 1028 is obtained at a wavelength of 1542 nm. The polarization dependence is also investigated. Figure 4d shows the normalized reflection intensity of the sample by rotating the polarization of the on-resonance laser. When the electric field is polarized predominantly along the y-axis, the reflection intensity reaches the maximum. A linear polarization dependence is 0.83, implying its high polarization sensitivity.

Now, we focus on the SHG from the samples. The sample is pumped by a pico-second pulsed laser (8.8 ps, 18.5 MHz), and the reflected SHG is collected and sent to a visible spectrometer. **Figure 5**a compares the measured SHG spectra from the fabricated sample and LNOI substrate. The integrated structure achieves an obvious enhancement in SHG and the enhancement factor is 25.4. SHG intensities at different pump powers under the illumination of an on-resonance laser are displayed in Figure 5b. The log-log plot shows a typical SHG effect owing to a quadratic slope (1.97 ± 0.03). The corresponding polarization dependence is plotted in Figure 5c. The polarization pattern is similar to that of the resonance mode. It indicates that the nonlinear response is affected by the mode sustained in the structure. The extinction ratio of the SHG polarization dependence reaches 0.98, which is much higher than that of the resonance mode. It can be qualitatively understood by considering that the SHG process has a quadratic function of the pump light. Figure 5d shows the wavelength dependence of the SHG intensity. The SHG intensity increases with the pump wavelength first and reaches a pronounced maximum at the resonance wavelength (i.e., 1542 nm), then reduces to lower. A significant attenuation in the SHG intensity occurs once the pump wavelength is away from the resonance wavelength. The SHG enhancement

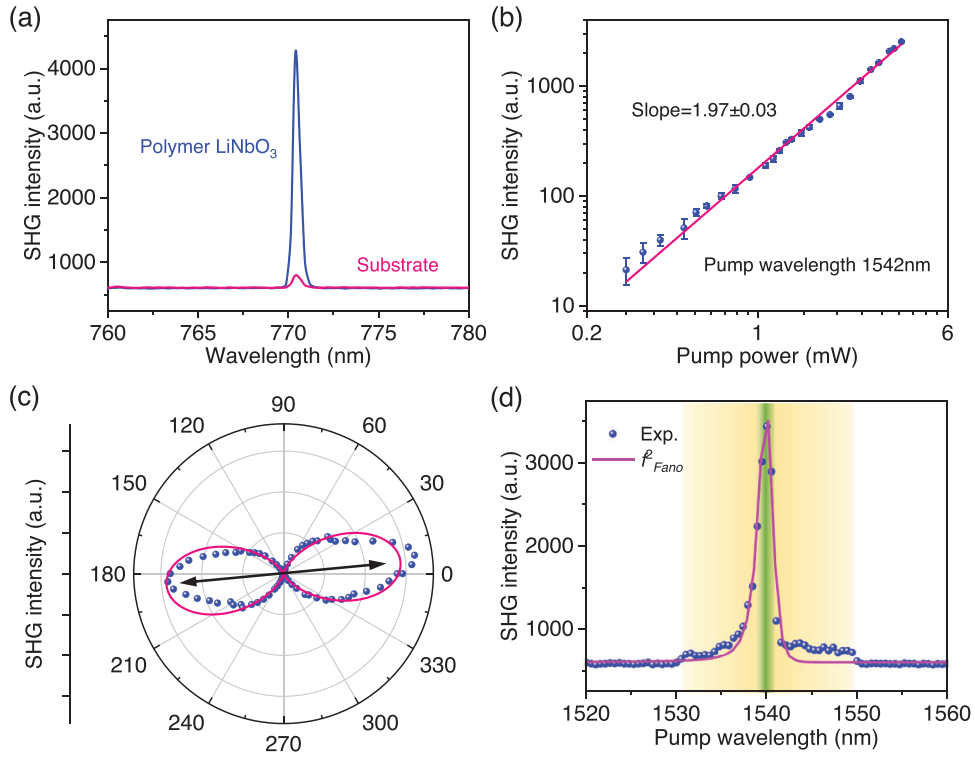

Figure 5. a) Experimentally measured SHG spectra from the LNOI with/without polymer nanocubes. b) Log-log plot of SHG intensities at different pump powers (blue error bars) and their linear fitting (pink line). c) Normalized polarization-dependent SHG intensities with the excitation of an on-resonance laser. The black arrow indicates the *y*-direction. d) Wavelength-dependent SHG intensities when the pump wavelength is tuned across the resonance wavelength. The yellow and green blurred areas represent the off-resonant and on-resonant coupling conditions, respectively.

originates from the field enhancement at the resonance condition. For the nonlinear response, the intensities of the *n*-order harmonic generation scale approximately with the factor $(Q/V)^n$.[34] SHG can be further enhanced by improving the *Q* factor. Additionally, the thickness of the polymer can be optimized to reduce the loss of the SH signal.

As discussed, the integrated structure hosts four optical modes and is capable of improving the light-matter interaction (i.e., SHG enhancement). To avoid the fabrication difficulty, several designs have been used for etchless-LN metasurfaces,[14,53–55] such as nanodisks,[14] photonic crystals,[53] and gratings.[54,55] Compared with them, our demonstrated LN metasurface exhibits the largest *Q* factors (see Table S1, Supporting Information). SHG can be further improved by optimizing the dimensions and materials of the nanocubes. In terms of preparation, polymer nanocubes are easy to implement. The proposed structure can promote the development of high-performance LN metadevices.

Furthermore, the diverse spectral characteristics are beneficial to multifunctionality. Three degrees of freedom (polarization, incident angle, and slot) are exploited to switch the operating mode, as shown in **Table 1**. Mode 1 and Mode 4 retain many properties of the conventional GMs while keeping appreciable *Q* factors.[38] By simply choosing the input polarization, single or multiple modes are excited, benefiting applications like multi-band filtering and polarization optics. Under TM-polarized wave, Mode 2 and Mode 3 remain high *Q* factors even at the large perturbation. It reduces the difficulties of applying symmetry-protected BIC in specific applications. At the oblique incidence, Mode 2 and Mode 4 are "filtered out" since they shift rapidly and are away from the operating wavelength. Thus Mode 3 is studied in this situation. The high-*Q* feature makes it suitable for improving light-matter interaction such as sensing, emission enhancement,[56] and nonlinear optics.[51,57] When the slot is introduced under the normal incidence, Mode 2 shows the highest *Q* factor, different from those of Mode 3 and Mode 4. The wavelength-selective multifunctionality is obtained. Upon the illumination of an oblique incident light, Mode 2, Mode 3, and Mode 4 are working simultaneously, which can support multiple-band applications.

Table 1. The operating mode of the integrated metasurface at different degrees of freedom.

Polarization	TE	TM		
Degree of Freedom	-	Angular	Slot	Angular&Slot
Operating Mode	Mode 1	Mode 3	Mode 2/3/4	Mode 2/3/4
			different *Q* factor	Similar *Q* factor
Function	Filtering	Sensing,	Wavelength-selective	Multiband Application
		Emission Enhancement,		
		Nonlinear Optics		

For practical application, different metasurfaces, including nanocubes with/without slots, are fabricated on the same LN substrate. The in-plane anisotropy of LN provides possibilities for band splitting. After introducing desirable optical modes, diverse spectral characteristics are obtained. This design principle is generic, i.e., different materials incorporated with LN can achieve multiple modes. In this case, the preparation of the multimode metasurface is available and easy. With elaborate design of arrays, different functionalities are integrated into a single device. For the degree of input polarization, the device automatically performs the corresponding function. When it comes to positions (i.e., different nanocubes) or angles, the device only exhibits multifunctionality at specific positions or angles. It is necessary to achieve the translation (positions) and rotation (angles) of the device. A combination of the multimode metasurface and electrically driven movable stage can be a simple approach to achieving multifunctionality. Limited by the present spectral characterizations, it can only achieve four different working states. We believe that the devices are able to support more functionality by adjusting the structure design and materials. The operating wavelength can be tuned by scaling the structure dimensions, which largely enriches the applicability and practicality (see Figure S6 in Supporting Information). In light of the simple and complementary metal-oxide-semiconductor (CMOS) compatible process, in-situ integration with other systems is also available, as a supplement for present microelectronic technologies.[58]

4. Conclusion

In summary, we theoretically proposed and experimentally demonstrated multiple optical modes in an integrated metasurface. A simple method is adopted to achieve the integrated structure by placing polymer nanocubes on the LN thin film. Nanocubes not only couple the guide mode to the far field but also yield an array effect to enhance Mie modes. Four modes with different spectral characteristics are obtained in the integrated metasurface. The experimentally measured Q factors of four modes are larger than 1000. The nonlinear characterization further confirms its ability to improve the light-matter interaction (i.e., SHG enhancement factor reaches 25.4). Diverse spectral characteristics introduce three degrees of freedom, including polarization, incident angle, and slot. By exploiting these degrees, mode selection is available, enabling the multifunctionality of the metasurface. We believe that our work delivers new insights into the realization of multimode metasurfaces with the simple method, enabling a compelling candidate for next-generation multifunctional flat-optics devices.

5. Experimental Section

Numerical Simulations: The numerical calculation of the polymer-LN integrated metasurface by utilizing the finite element method (COMSOL Multiphysics) was performed. In all simulations, a single polymer nanocube placed on an LN/SiO_2 substrate was simulated in the *x*-*y* plane with periodic boundary conditions.[59] Perfect matching layers were employed in the *z* direction to eliminate unwanted reflection. In solving the frequency-domain problem, the TE/TM wave was illuminated along the *z*-axis with polarization along the *y*/*x*-axis. The refractive index of the silica and polymer were set to 1.44 and 1.67, respectively. Given the anisotropic nature of the LN, constant refractive indices of $n_y = n_e = 2.14$ and $n_x = n_z = n_o = 2.21$ were defined, meaning that the optical axis was along the y direction. The Q factors and mode simulations were evaluated by the eigenfrequency solver. The reflection spectra were calculated in the frequency domain calculation.

Sample Fabrication: In the experiment, a 400 nm-thick *x*-cut LNOI wafer was adopted. The wafer was diced into 1 cm × 1 cm pieces, which were cleaned sequentially in N-methyl-2-pyrrolidone (90 °C), isopropyl alcohol (ultrasonic cleanout), deionized water (ultrasonic cleanout), and piranha solution (90 °C) for 10 min, respectively. After that, AR-P 6200.13 was spun on the sample at 4000 rpm to obtain a thickness of 400 nm. The sample was then baked on a hot plate at 180 °C for 3 min. Electron beam lithography was performed on the samples to transfer the pattern on the resist. At last, the residual resist was removed with the developer.

Optical Characterizations: The samples were characterized using a home-built setup with a reflection configuration. For linear optical responses, a broadband supercontinuum laser (YSL photonics, SC-Pro) was focused on the sample. The reflected light was collected by an objective (20×/0.4 or 2×/0.055), which was finally coupled to an infrared spectrometer (Andor tech., DU490A-1.7). The NA of an objective determines its ability to focus light and the acceptance angle for the signal collection. To characterize the Q factor more clearly, samples were illuminated by a narrowband tunable laser (Yenista Tunics T100S-HP), and reflected signals were measured using a telecom-band photodiode. The measured data were fitted by the Fano function $f_{\text{Fano}} = ((q+(\omega-\omega_0)/\gamma)^2+\gamma^2)/(1+((\omega-\omega_0)/\gamma)^2)$ to obtain the accurate value of the Q factor.[60] Here q was the asymmetry factor, ω_0 was the resonance wavelength, and γ represents the damping rate. The Q factor was calculated by $Q/2\gamma$. The SH signals were collected and coupled to a visible spectrometer (Princeton Instruments, SP 2558 & 100BRX) when pumped by a fiber-based pulsed laser with a pulse width of 8.8 ps and a repetition rate of 18.5 MHz. During the measurement, a polarizer and a half-wave plate were utilized to control the linear polarization of the pump laser illuminated on the sample. The power of the pump laser was adjusted by an optical attenuator.

Supporting Information

Supporting Information is available from the Wiley Online Library or from the author.

Acknowledgements

The authors acknowledge support from the National Key R&D Program of China (no. 2022ZD0119002 and 2022YFA1404800), the National Natural Science Foundation of China (grant no. 62025402, 62090033, 91964202, 92064003, 92264202, 62293522, 62375225, and 12374359) and Major Program of Zhejiang Natural Science Foundation (grant no. DT23F0402), the Fundamental Research Funds for the Central Universities (grant no. QTZX23040 and QTZX23079), and the Natural Science Basic Research Program of Shaanxi (Program No. 2023JC-XJ-01).

Conflict of Interest

The authors declare no conflict of interest.

Data Availability Statement

The data that support the findings of this study are available on request from the corresponding author.

Keywords

bound states in the continuum, etchless lithium niobate, guided mode, integrated metasurface, multimode

Received: September 13, 2023
Revised: October 18, 2023
Published online: November 22, 2023

[1] G. Li, S. Zhang, T. Zentgraf, *Nat. Rev. Mater.* **2017**, *2*, 17010.
[2] S. Chen, W. Liu, Z. Li, H. Cheng, J. Tian, *Adv. Mater.* **2020**, *32*, 1805912.
[3] Q. He, S. Sun, S. Xiao, L. Zhou, *Adv. Opt. Mater.* **2018**, *6*, 1800415.
[4] H. Gao, X. Fan, W. Xiong, M. Hong, *Opto-Electron. Adv.* **2021**, *4*, 210030.
[5] C.-W. Qiu, T. Zhang, G. Hu, Y. Kivshar, *Nano Lett.* **2021**, *21*, 5461.
[6] H. Wang, C. Hao, H. Lin, Y. Wang, T. Lan, C.-W. Qiu, B. Jia, *Opto-Electron. Adv* **2021**, *4*, 200031.
[7] D. R. Gozzard, L. E. Roberts, J. T. Spollard, P. G. Sibley, D. A. Shaddock, *Opt. Lett.* **2020**, *45*, 3793.
[8] W. T. Buono, A. Forbes, *Opto-Electron. Adv* **2022**, *5*, 210174.
[9] X. Hong, K. Wang, C. Guan, X. Han, Y. Chen, S. Qian, X. Xing, C.-W. Qiu, P. Lu, *Nano Lett.* **2022**, *22*, 8860.
[10] J. Liu, M. Shi, Z. Chen, S. Wang, Z. Wang, S. Zhu, *Opto-Electron. Adv.* **2021**, *4*, 200092.
[11] K. Liu, M. Lian, K. Qin, S. Zhang, T. Cao, *Light: Adv. Manuf.* **2021**, *2*, 19.
[12] Y. Che, X. Wang, Q. Song, Y. Zhu, S. Xiao, *Nanophotonics* **2020**, *9*, 4407.
[13] X. Zang, B. Yao, L. Chen, J. Xie, X. Guo, A. V. Balakin, A. P. Shkurinov, S. Zhuang, *Light: Adv. Manuf.* **2021**, *2*, 10.
[14] A. Weiss, C. Frydendahl, J. Bar-David, R. Zektzer, E. Edrei, J. Engelberg, N. Mazurski, B. Desiatov, U. Levy, *ACS Photonics* **2022**, *9*, 605.
[15] B.o Xiong, L. Deng, R. Peng, Y. Liu, *Nanoscale Adv.* **2019**, *10*, 3786.
[16] S. Kruk, Y. Kivshar, *ACS Photonics* **2017**, *4*, 2638.
[17] A. I. Kuznetsov, A. E. Miroshnichenko, M. L. Brongersma, Y. S. Kivshar, B. Luk'yanchuk, *Science* **2016**, *354*, aag2472.
[18] S. Li, B. Ma, Q. Li, M. V. Rybin, *Nanophotonics* **2022**, *11*, 4843.
[19] Z. Li, T. Wu, X. Zhang, *Optics Lett.* **2019**, *44*, 57.
[20] J. Jeong, M. D. Goldflam, S. Campione, J. L. Briscoe, P. P. Vabishchevich, J. Nogan, M. B. Sinclair, T. S. Luk, I. Brener, *ACS Photonics* **2020**, *7*, 1699.
[21] Y. Yang, V. A. Zenin, S. I. Bozhevolnyi, *ACS Photonics* **2018**, *5*, 1960.
[22] J. A. Garcia, C. Hrelescu, X. Zhang, D. Grosso, M. Abbarchi, A. L. Bradley, *ACS Appl. Mater. Interfaces* **2021**, *13*, 47860.
[23] J. Jang, T. Badloe, Y. Yang, T. Lee, J. Mun, J. Rho, *ACS Nano* **2020**, *14*,15317.
[24] Y. Yang, A. E. Miroshnichenko, S. V. Kostinski, M. Odit, P. Kapitanova, M. Qiu, Y. S. Kivshar, *Phys. Rev. B* **2017**, *95*, 165426.
[25] X. Du, L. Xiong, X. Zhao, S. Chen, J. Shi, G. Li, *Nanophotonics* **2022**, *11*, 4843.
[26] S. Murai, G. W. Castellanos, T. V. Raziman, A. G. Curto, J. G. Rivas, *Adv. Opt. Mater.* **2020**, *8*, 1902024.
[27] D. Hähnel, C. Golla, M. Albert, T. Zentgraf, V. Myroshnychenko, J. Förstner, C. Meier, *Light: Sci. Appl.* **2023**, *12*, 97.
[28] B.o Yang, W. Liu, Z. Li, H. Cheng, D.-Y. Choi, S. Chen, J. Tian, *Nano Lett.* **2019**, *19*, 4221.
[29] Y. Shen, S. Xue, G. Dong, J. Yang, S. Hu, *Adv. Opt. Mater.* **2021**, *9*, 2101340.
[30] L. Wang, I. Shadrivov, *Opt. Exp.* **2022**, *30*, 35361.
[31] H. Liu, B. Pan, Y. Huang, J. He, M. Zhang, Z. Yu, L. Liu, Y. Shi, D. Dai, *Light: Adv. Manuf.* **2023**, *4*, 13.
[32] C. W. Hsu, B.o Zhen, A. D. Stone, J. D. Joannopoulos, M. Soljacic, *Nat. Rev. Mater.* **2016**, *1*, 16048.
[33] K. Koshelev, S. Lepeshov, M. Liu, A. Bogdanov, Y. Kivshar, *Phys. Rev. Lett.* **2018**, *121*, 193903.
[34] C. Fang, Q. Yang, Q. Yuan, X. Gan, J. Zhao, Y Shao, Y. Liu, G. Han, Y. Hao, *Opto-Electron. Adv.* **2021**, *4*, 200030.
[35] H. M. Doeleman, F. Monticone, W. Den Hollander, A. Alù, A. F. Koenderink, *Nat. Photonics* **2018**, *12*, 397.
[36] S. Mohamed, J. Wang, H. Rekola, J. Heikkinen, B. Asamoah, L. Shi, T. K. Hakala, *Laser Photonics Rev.* **2022**, *16*, 2100574.
[37] B.o Zhen, C. W. Hsu, L. Lu, A. D. Stone, M. Soljacic, *Phys. Rev. Lett.* **2014**, *113*, 257401.
[38] K. Sun, H. Wei, W. Chen, Y. Chen, Y. Cai, C.-W. Qiu, Z. Han, *Phys. Rev. B* **2023**, *107*, 115415.
[39] S. G. Tikhodeev, A. L. Yablonskii, E. A. Muljarov, N. A. Gippius, T. Ishihara, *Phys. Rev. B* **2002**, *66*, 045102.
[40] S. Han, M. V. Rybin, P. Pitchappa, Y. K. Srivastava, Y. S. Kivshar, R. Singh, *Adv. Opt. Mater.* **2020**, *8*, 1900959.
[41] L. Huang, R. Jin, C. Zhou, G. Li, L. Xu, A. Overvig, F. Deng, X. Chen, W. Lu, A. Alù, A. E. Miroshnichenko, *Nat. Commun.* **2023**, *14*, 3433.
[42] M. Wu, S. T. Ha, S. Shendre, E. G. Durmusoglu, W.-K. Koh, D. R. Abujetas, J. A. Sánchez-Gil, R. Paniagua-Domínguez, H. V. Demir, A. I. Kuznetsov, *Nano Lett.* **2020**, *20*, 6005.
[43] J. Tian, G. Adamo, H. Liu, M. Wu, M. Klein, J. Deng, N. S. S. Ang, R. Paniagua-Domínguez, H. Liu, A. I. Kuznetsov, C. Soci, *Adv. Mater.* **2023**, *35*, 2207430.
[44] R. Heilmann, G. Salerno, J. Cuerda, T. K. Hakala, P. Torma, *ACS Photonics* **2022**, *9*, 224.
[45] T. Kaelberer, V. A. Fedotov, N. Papasimakis, D. P. Tsai, N. I. Zheludev, *Science* **2010**, *330*, 1510.
[46] A. Tripathi, H.a-R. Kim, P. Tonkaev, S.-J. Lee, S. V. Makarov, S. S. Kruk, M. V. Rybin, H.-G. Park, Y. Kivshar, *Nano Lett.* **2021**, *21*, 6563.
[47] Z. Sadrieva, K. Frizyuk, M. Petrov, Y. Kivshar, A. Bogdanov, *Phys. Rev. B* **2019**, *100*, 115303.
[48] W. Chen, Y. Chen, W. Liu, *Phys. Rev. Lett.* **2019**, *122*, 153907.
[49] S. Campione, S. Liu, L. I. Basilio, L. K. Warne, W. L. Langston, T. S. Luk, J. R. Wendt, J. L. Reno, G. A. Keeler, I. Brener, M. B. Sinclair, *ACS Photon* **2016**, *3*, 2362.
[50] Z. Liu, Y.i Xu, Y.e Lin, J. Xiang, T. Feng, Q. Cao, J. Li, S. Lan, J. Liu, *Phys. Rev. Lett.* **2019**, *123*, 253901.
[51] C. Fang, Q. Yang, Q. Yuan, L. Gu, X. Gan, Y. Shao, Y. Liu, G. Han, Y. Hao, *Laser Photonics Rev.* **2022**, *16*, 2100498.
[52] Y. Yu, Z. Yu, L. Wang, X. Sun, *Adv. Opt. Mater.* **2021**, *9*, 2100060.
[53] Z. Huang, K. Luo, Z. Feng, Z. Zhang, Y. Li, W. Qiu, H. Guan, Y.i Xu, X. Li, H. Lu, *Sci. China-Phys. Mech. Astron.* **2022**, *65*, 104211.
[54] X. Chen, R. Leng, K. Liu, C. Guo, Z. Zhu, S. Qin, J. Zhang, *Opt. Laser Technol.* **2023**, *161*, 109163.
[55] Y. Hu, Z. Huang, X. Zeng, Y. Li, K. Luo, H. Guan, Y. Cao, H. Lu, *Opt. Mater. Express* **2023**, *13*, 2904.
[56] S. Yuan, X. Qiu, C. Cui, L. Zhu, Y. Wang, Y. Li, J. Song, Q. Huang, J. Xia, *ACS Nano* **2017**, *11*, 10704.
[57] T. A. K. Lühder, H. Schneidewind, E. P. Schartner, H. Ebendorff-Heidepriem, M. A. Schmidt, *Light: Adv. Manuf.* **2021**, *2*, 21.
[58] Y. Zhu, X. Zang, H. Chi, Y. Zhou, Y. Zhu, S. Zhuang, *Light: Adv. Manuf.* **2023**, *4*, 9.
[59] C. Fang, Y. Liu, G. Han, Y. Shao, J. Zhang, Y. Hao, *Opt. Exp.* **2018**, *26*, 27683.
[60] I. Avrutsky, R. Gibson, J. Sears, G. Khitrova, H. M. Gibbs, J. Hendrickson, *Phys. Rev. B* **2013**, *87*, 125118.

